

A 2D Discontinuous Galerkin Method for Aeroacoustics with Curved Boundary Treatment

Thomas Toulorge*, Yves Reymen† and Wim Desmet‡

K.U. Leuven, Dept. of Mechanical Engineering, Celestijnenlaan 300, B-3001 Heverlee, Belgium

Abstract

A Discontinuous Galerkin Method is applied to unstructured grids to simulate aeroacoustic propagation, modelled by the Linearized Euler Equations. The quadrature-free form of the Discontinuous Galerkin Method is used on triangular elements with straight edges. Computations of a freely propagating pressure pulse demonstrate that the implementation achieves the theoretical order of accuracy. With increasing order, the method becomes more efficient. However, simulation of acoustic scattering by a cylinder shows that the linear treatment of the geometry can limit the accuracy at high order. Two higher-order treatments of curved boundaries are presented to overcome this restriction. It is found that only the use of curved elements, on which the quadrature-free technique cannot be applied, provides satisfying accuracy; further implications on stability and computational cost are discussed.

1 Introduction

The noise generated by internal or external flow encountered in industrial machinery can cause shorter machine life, lower environmental performance, and user discomfort. As a result, the interest for aeroacoustics has grown dramatically in the last few decades, and the demand for prediction capabilities of flow-generated noise is increasing. In this context, computational aeroacoustics (CAA) is beneficial to designers of industrial products by limiting the need for expensive and time-consuming test campaigns.

Although the numerical study of flow-generated sound can be seen as a research field within Computational Fluid Dynamics (CFD), it features several specificities due to the different nature of the sound and its generating flow: the amplitude of acoustical perturbations is usually much smaller than the one of the flow, and their typical length scale much larger. Moreover, their frequency spectra can be very broad, and they can propagate over large distances. Therefore, dedicated numerical schemes with low dissipation and dispersion properties are required to accurately model these phenomena. Along with the need for high accuracy, the intrinsic unsteady character of aeroacoustic problems lead to high computational costs.

Two approaches can be considered to compute flow-generated noise. The so-called "direct" approach consists in performing a CFD computation that is accurate enough to capture both aerodynamics and acoustics with a minimal production of "numerical noise". This method, usually carried out by using high-order or spectral methods in conjunction with LES or DNS models, is still computationally very expensive, especially for complex geometries [1]. A more pragmatic approach, the "hybrid" methodology, consists in performing an accurate CFD computation only in the region where flow noise is generated, and calculating the propagation

*Ph.D. Student

†Ph.D. Student

‡Professor

of the resulting sound in the whole domain of interest with a separate numerical method. It cannot be applied to problems with strong coupling between aerodynamics and acoustics (i.e. problems in which the acoustic perturbations affect the behaviour of the flow). This approach is usually less computationally intensive.

This paper focuses on the Discontinuous Galerkin Method (DGM) applied to the Linearized Euler Equations (LEE) for the computation of acoustic propagation. It was introduced by Reed and Hill [2] to simulate neutron transport and has been applied to numerous equations since then, particularly in the fields of Electromagnetism and Fluid Dynamics. Just as the continuous Finite Element Method (FEM), it consists in representing the local quantities in each element of the grid by a projection on a suitable basis (most often polynomials), and applying the Galerkin procedure to the governing Partial Differential Equation. But, in contrast to traditional FEM, where the continuity of variables between elements is imposed, DGM allows the solution to be discontinuous at element boundaries. Conservation is then enforced through the use of a flux at element boundaries, where a Riemann problem is solved, in the manner of Finite Volume Methods. This construction features an arbitrary order of accuracy, which only depends on the order of the underlying polynomial basis, while maintaining an extreme compactness: the only non-local information used in the scheme comes from the communication between an element and its neighbours. Along with the ability to handle unstructured grids, and the straightforward formulation of boundary conditions through the flux formulation, these properties are clear advantages over the Finite Difference (FD) schemes traditionally used to solve the LEE for CAA applications. However, DGM has been criticized for two reasons that make it computationally expensive compared to FD methods: discontinuous solutions require extra degrees of freedom, and the method involves integration of higher-order functions, which is traditionally carried out through quadrature. The latter was palliated by Atkins and Shu [3] when introducing the quadrature-free form of DGM, which consists in mapping all elements in the physical domain onto a single reference element for which the integration of base function products is pre-computed. This technique is subject to certain constraints on the geometry of physical elements (e.g. straight edges for triangles or flat faces for tetrahedra).

Several authors have investigated the application of DGM to wave propagation problems. In particular, the behaviour of DGM with respect to dissipation and dispersion has been well studied by means of theory and numerical experiments [4, 5, 6, 7]. The influence of h- and p-refinement on the accuracy of DGM [8, 9], as well as the discretization error on different kinds of grids [10, 11], were investigated. Several authors report the successful application of DGM to Maxwell's equations [12] and to aeroacoustic problems [13, 14, 15]. However, these works do not include the study of the error that is due to the discretization of the geometry.

In the framework of the non-linear Euler equations, the necessity of a higher-order treatment of curved wall boundaries was put in evidence by Bassy and Rebay [16], and is now generally accepted [17]. Ref. [16] and [17] suggest that the accuracy mainly depends on the correct representation of the normals to the geometry, when dealing with 2D Euler flows. However, this might not be the case with acoustic propagation problems. Concerning the LEE, Atkins reported the use of higher-order geometry description and its benefits on problems of acoustic scattering [18].

In the present work, DGM is applied to the LEE in 2D to simulate aeroacoustic propagation on triangular grids, with the objective of studying the influence of boundary treatment for curved walls. The implementation is first verified with the case of a Gaussian pressure pulse propagating in free field. Then a problem of acoustic scattering by a 2D cylinder is used to show how the linear treatment of wall boundaries limits the accuracy. The benefits of two different boundary treatments based on higher-order geometry representation are evaluated for this case.

The numerical method is described in Section 2, and the results of the two test problems are discussed in Section 3. Conclusions are drawn in Section 4.

2 Method

The approach taken here is based on the work of Reymen [11, 19], who uses a nodal DGM on tetrahedral and hexahedral grids, combined with a low-storage fourth-order-accurate Runge-Kutta scheme [21] for time

integration. This method was successfully applied to the LEE in the framework of aeroacoustic simulations. In the present work, this approach is used in 2D and extended to curved triangular elements to model curved wall boundaries, with the purpose of overcoming the limitations of linear geometry treatment which are put in evidence in Section 3.

2.1 Governing Equations

The governing equations are the 2D linearized Euler equations, that are capable of solving acoustic propagation in non-uniform flows:

$$\frac{\partial \mathbf{q}}{\partial t} + \frac{\partial \mathbf{F}_r}{\partial x_r} + \mathbf{C}\mathbf{q} = \mathbf{s} \quad (1)$$

where

$$\mathbf{q} = \begin{bmatrix} \rho \\ \rho_0 u_1 \\ \rho_0 u_2 \\ p \end{bmatrix}$$

$$\mathbf{F}_r = \mathbf{A}_r \mathbf{q} = \begin{bmatrix} u_{0r} & \delta_{1r} & \delta_{2r} & 0 \\ 0 & u_{0r} & 0 & \delta_{1r} \\ 0 & 0 & u_{0r} & \delta_{2r} \\ 0 & \frac{\gamma p_0}{\rho_0} \delta_{1r} & \frac{\gamma p_0}{\rho_0} \delta_{2r} & u_{0r} \end{bmatrix} \mathbf{q}$$

$$\mathbf{C} = \begin{bmatrix} 0 & 0 & 0 & 0 \\ u_{0r} \frac{\partial u_{01}}{\partial x_r} & \frac{\partial u_{01}}{\partial x_1} & \frac{\partial u_{01}}{\partial x_2} & 0 \\ u_{0r} \frac{\partial u_{02}}{\partial x_r} & \frac{\partial u_{02}}{\partial x_1} & \frac{\partial u_{02}}{\partial x_2} & 0 \\ 0 & \frac{(1-\gamma)}{\rho_0} \frac{\partial p_0}{\partial x_1} & \frac{(1-\gamma)}{\rho_0} \frac{\partial p_0}{\partial x_2} & (\gamma - 1) \frac{\partial u_{0r}}{\partial x_r} \end{bmatrix}$$

Here r is one of the two cartesian coordinates ($x_1 \equiv x$, $x_2 \equiv y$) on which Einstein's summation convention is used; \mathbf{s} is the acoustic source vector; (ρ, u_1, u_2, p) are respectively the acoustic perturbations in density, x-velocity, y-velocity and pressure, and $(\rho_0, u_{10}, u_{20}, p_0)$ are the corresponding quantities for the mean flow; γ is the heat capacity ratio and δ_{ij} is the Kronecker delta. The term $\mathbf{C}\mathbf{q}$ accounts for non-uniform mean flow effects.

2.2 Spatial Discretization

In this work, DGM is applied to unstructured triangular meshes. The computational domain is paved with straight-edge triangles, on which the quadrature-free form of DGM is applied. Optionally, curved elements and edges, that require the use of quadrature, can be employed near wall boundaries where the geometry is described by a quadratic equation.

2.2.1 Formulation

For each element Ω of the grid, a basis $\mathcal{B} = \{\varphi_j, j = 1 \dots N_p\}$ is defined, in which the components φ_j are polynomials of order p supported by Ω , with $N_p = \frac{(p+1)(p+2)}{2}$ for triangular elements. An approximation \mathbf{q}^Ω of the vector of variables \mathbf{q} on Ω is obtained by a projection on this basis:

$$\mathbf{q}^\Omega = \sum_{j=1}^{N_p} \mathbf{q}_j^\Omega \varphi_j$$

Applying the Galerkin procedure to Eq. (1) with $\mathbf{s} = 0$ and $\mathbf{C} = 0$, and using Green-Gauss theorem, results in:

$$\int_{\Omega} \varphi_k \sum_{j=1}^{N_p} \frac{\partial \mathbf{q}_j^\Omega}{\partial t} \varphi_j d\Omega - \int_{\Omega} \frac{\partial \varphi_k}{\partial x_r} \sum_{j=1}^{N_p} \mathbf{F}_{\mathbf{r}j}^\Omega \varphi_j d\Omega + \int_{\partial\Omega} \varphi_k \sum_{j=1}^{N_p} \mathbf{F}_{\mathbf{R}j}^{\partial\Omega} \varphi_j d\partial\Omega = 0, \quad k = 1 \dots N_p \quad (2)$$

where $\mathbf{F}_{\mathbf{r}}^\Omega$ is a projection of $\mathbf{F}_{\mathbf{r}}$ on \mathcal{B} , and $\mathbf{F}_{\mathbf{R}}^{\partial\Omega}$ is a projection on \mathcal{B} of the Riemann flux computed on the element boundary $\partial\Omega$ as:

$$\mathbf{F}_{\mathbf{R}}^{\partial\Omega} = \frac{1}{2} \left[\left(\mathbf{F}_{\mathbf{r}}^\Omega + \mathbf{F}_{\mathbf{r}}^{\Omega'} \right) n_r - \alpha \left(\mathbf{q}^\Omega + \mathbf{q}^{\Omega'} \right) \right] \quad (3)$$

α is the maximum eigenvalue of $\frac{\partial \mathbf{F}}{\partial \mathbf{q}}$, n_r is the r-component of the local outgoing normal to the boundary $\partial\Omega$, $\mathbf{q}^{\Omega'}$ and $\mathbf{F}_{\mathbf{r}}^{\Omega'}$ are the equivalents of \mathbf{q}^Ω and $\mathbf{F}_{\mathbf{r}}^\Omega$ respectively in the element Ω' locally sharing $\partial\Omega$ with Ω . Following the quadrature-free form of DGM [3], all elements in the physical domain can then be mapped onto a single reference element Δ :

$$\mathcal{M}^\Omega : \begin{array}{ccc} \Delta & \rightarrow & \Omega \\ (\xi_1, \xi_2) & \mapsto & (x_1, x_2) \end{array}$$

The Jacobian matrix of \mathcal{M}^Ω is then defined by $J_{ij}^\Omega = \frac{\partial x_i}{\partial \xi_j}$, and the change of coordinates in Eq. (2) yields:

$$\begin{aligned} \int_{\Delta} \varphi_k \sum_{j=1}^{N_p} \frac{\partial \mathbf{q}_j^\Omega}{\partial t} \varphi_j |J^\Omega| d\Delta - \int_{\Delta} (J^\Omega)^{-1}_{sr} \frac{\partial \varphi_k}{\partial \xi_s} \sum_{j=1}^{N_p} \mathbf{F}_{\mathbf{r}j}^\Omega \varphi_j |J^\Omega| d\Delta \\ + \int_{\partial\Delta} \varphi_k \sum_{j=1}^{N_p} \mathbf{F}_{\mathbf{R}j}^{\partial\Omega} \varphi_j |J^{\partial\Omega}| d\partial\Delta = 0, \quad k = 1 \dots N_p \quad (4) \end{aligned}$$

where $J^{\partial\Omega}$ is the Jacobian matrix of the mapping of $\partial\Omega$ on $\partial\Delta$. Eq. (4) can then be rewritten in a matrix form:

$$\mathbf{M}^\Omega \frac{\partial \mathbf{q}^\Omega}{\partial t} - \mathbf{K}_{\mathbf{r}}^\Omega \mathbf{F}_{\mathbf{r}}^\Omega + \sum_{i=1}^3 \mathbf{M}^{\partial\Omega_i} \mathbf{F}_{\mathbf{R}}^{\partial\Omega_i} = 0 \quad (5)$$

with $\partial\Omega_i$ corresponding to the edge i of Ω , and:

$$\begin{aligned} \mathbf{M}_{kj}^\Omega &= \int_{\Delta} \varphi_k \varphi_j |J^\Omega| d\Delta \\ (\mathbf{K}_{\mathbf{r}}^\Omega)_{kj} &= \int_{\Delta} (J^\Omega)^{-1}_{sr} \frac{\partial \varphi_k}{\partial \xi_s} \varphi_j |J^\Omega| d\Delta \\ \mathbf{M}_{kj}^{\partial\Omega_i} &= \int_{\partial\Delta_i} \varphi_k \varphi_j |J^{\partial\Omega_i}| d\partial\Delta_i \end{aligned} \quad (6)$$

In this work, the basis functions φ_j are Lagrange polynomials based on a nodal set that reduces to Lagrange-Gauss-Lobatto points on the edges [20]. Thus \mathcal{B} reduces to a basis of one-dimensional polynomials on $\partial\Omega_i$, which can be used to store lower-rank matrices for $\mathbf{M}^{\partial\Omega_i}$ and $\mathbf{F}_{\mathbf{R}}^{\partial\Omega_i}$. Integrals are computed on an polynomial basis that is orthogonal in Δ , following the work of Hesthaven and Warburton [12].

2.2.2 Elements with Straight Edges

Interior elements are triangles with straight edges, so that J^Ω and $J^{\partial\Omega}$ are constant over Δ and $\partial\Delta$ respectively, and can be taken out of the integrals in Eq. (6):

$$\begin{aligned}\mathbf{M}^\Omega &= |J^\Omega| \mathbf{M}^\Delta \\ \mathbf{K}_{\mathbf{r}}^\Omega &= (J^\Omega)_{sr}^{-1} |J^\Omega| \mathbf{K}_{\mathbf{s}}^\Delta \\ \mathbf{M}^{\partial\Omega_i} &= |J^{\partial\Omega_i}| \mathbf{M}^{\partial\Delta_i}\end{aligned}$$

with:

$$\begin{aligned}\mathbf{M}_{kj}^\Delta &= \int_{\Delta} \varphi_k \varphi_j d\Delta \\ (\mathbf{K}_{\mathbf{s}}^\Delta)_{kj} &= \int_{\Delta} \frac{\partial \varphi_k}{\partial \xi_s} \varphi_j d\Delta \\ \mathbf{M}_{kj}^{\partial\Delta_i} &= \int_{\partial\Delta_i} \varphi_k \varphi_j d\partial\Delta_i\end{aligned}\tag{7}$$

The memory storage for each element and edge thus reduces to the Jacobian terms, given that \mathbf{M}^Δ , $\mathbf{K}_{\mathbf{s}}^\Delta$ and $\mathbf{M}^{\partial\Delta_i}$ can be precomputed. The use of an orthogonal basis in Δ , for which a transformation from \mathcal{B} is defined, allows an easy analytical computation of matrices in Eq. (7).

2.2.3 Curved Elements

In this work, the geometry can be described with quadratic polynomials. In this case, each edge $\partial\Omega_i$ lying on the curved wall boundary is mapped onto the reference edge by a quadratic function, and \mathcal{M}^Ω is also of order 2 for the corresponding elements. Then J^Ω and $J^{\partial\Omega_i}$ are no longer constant over Ω and $\partial\Omega_i$ respectively, and they cannot be taken out of the integrals in Eq. (6), which has two implications:

- Integration in Eq. (6) requires quadrature. In the present work, Gauss-Legendre quadrature rules are used to compute the matrices. Care is taken to choose rules of sufficiently high order to integrate exactly the products of polynomials that form the integrands.
- Integrals in Eq. (6) cannot be precomputed, so that \mathbf{M}^Ω and $\mathbf{K}_{\mathbf{r}}^\Omega$ are calculated and stored in memory for each element Ω of the grid, as well as $\mathbf{M}^{\partial\Omega_i}$ for each edge $\partial\Omega_i$. For these element and edges, the cost in memory is thus much higher than with the quadrature-free technique described in Section 2.2.2.

Also, the use of curved edges implies that the components n_r of the normal to $\partial\Omega_i$ in Eq. (3) are not constant. Thus, the projection of the Riemann flux on \mathcal{B} results in a truncation: as $\partial\Omega_i$ is described by a quadratic polynomial, the scalar product $(\mathbf{F}_{\mathbf{r}}^\Omega + \mathbf{F}_{\mathbf{r}}^{\Omega'}) n_r$ is of order $p + 1$, whereas $\mathbf{F}_{\mathbf{R}}^{\partial\Omega}$ is of order p . To prevent truncation, the terms in Eq. (3) have to be integrated separately and Eq. (5) then becomes:

$$\mathbf{M}^{\Omega} \frac{\partial \mathbf{q}^{\Omega}}{\partial t} - \mathbf{K}_{\mathbf{r}}^{\Omega} \mathbf{F}_{\mathbf{r}}^{\Omega} + \sum_{i=1}^3 \frac{1}{2} \left[\mathbf{M}_{\mathbf{r}}^{\partial \Omega_i} \left(\mathbf{F}_{\mathbf{r}}^{\Omega} + \mathbf{F}_{\mathbf{r}}^{\Omega'} \right) - \alpha \mathbf{M}^{\partial \Omega_i} \left(\mathbf{q}^{\Omega} + \mathbf{q}^{\Omega'} \right) \right] = 0$$

with:

$$(\mathbf{M}_{\mathbf{r}})_{kj}^{\partial \Omega_i} = \int_{\partial \Delta_i} \varphi_k \varphi_j n_r \left| J^{\partial \Omega_i} \right| d\partial \Delta_i$$

Thus three matrices $\mathbf{M}_1^{\partial \Omega_i}$, $\mathbf{M}_2^{\partial \Omega_i}$ and $\mathbf{M}^{\partial \Omega_i}$ have to be stored in memory for each edge $\partial \Omega_i$ to avoid truncation, instead of one. Although computationally more expensive, this treatment is slightly more accurate, therefore all results presented in this work are obtained with non-truncated Riemann fluxes.

2.3 Boundary Treatment

In this work, all boundary conditions are enforced in a "weak" manner by prescribing the fluxes at boundary. Walls are modelled by computing at each node of the boundary edge $\partial \Omega_i$ a modified flux that fulfills the condition:

$$\mathbf{u} \cdot \mathbf{N} = 0$$

with $\mathbf{u} = \begin{bmatrix} u_1 \\ u_2 \end{bmatrix}$, \mathbf{N} being either the normal \mathbf{n} to $\partial \Omega_i$, or the local normal $\mathbf{n}_{\mathbf{g}}$ to the quadratically-represented geometry. In this work, three different wall boundary treatments, illustrated in Fig. 1, are investigated:

- $\partial \Omega_i$ is a straight edge and $\mathbf{N} = \mathbf{n}$. In this case the treatment of wall boundaries is fully linear, and quadrature-free DGM is used, as described in Section 2.2.2.
- $\partial \Omega_i$ is a straight edge and $\mathbf{N} = \mathbf{n}_{\mathbf{g}}$. As in the linear case, quadrature-free DGM is used. This treatment, proposed in Ref. [16] and Ref. [17] as a "cheap" way to improve accuracy, will be hereafter referred to as "mixed".
- $\partial \Omega_i$ is a curved edge, in this case $\mathbf{N} = \mathbf{n} = \mathbf{n}_{\mathbf{g}}$ and the treatment is fully quadratic. Integration over the edge $\partial \Omega_i$ and the adjacent element Ω is then performed by quadrature, as explained in Section 2.2.3.

Far-field conditions on the outer domain boundaries are achieved by splitting the equations into characteristic solutions and suppressing ingoing waves.

3 Results

3.1 Gaussian Pressure Pulse

To verify the numerical method and its implementation, the free-field propagation of a Gaussian pressure pulse is simulated [22]. An analytical solution is available for this problem, that allows accurate comparison with numerical results.

The computational domain consists in a square of non-dimensional length 200, centered at the origin. The initial conditions are:

$$p|_{t=0} = \rho|_{t=0} = e^{-(\ln 2) \frac{x^2+y^2}{5^2}}$$

$$u_1|_{t=0} = u_2|_{t=0} = 0$$

The mean flow velocity is set to zero and the Gaussian pressure pulse is propagated until a non-dimensional time of $t = 20$. This ensures that the wave front remains inside the domain, to prevent the solution from being polluted by any spurious reflection at boundaries. Several grids, whose characteristics are summarized in Table 1, are used, with the order p of the polynomial basis varying from 1 to 6.

The error due to time discretization is negligible and the time step can be chosen in function of the stability condition on the CFL number, that is inversely proportional to the element size and depends on p . To avoid searching for the maximum time step preserving stability in each case, the same value is used for all computations. The computation time is thus not optimal, above all on coarser grids and at lower order.

| Grid Nr. | 1 | 2 | 3 | 4 |
|----------|-----|------|-------|-------|
| Vertices | 435 | 1654 | 6455 | 25519 |
| Elements | 868 | 3306 | 12908 | 50236 |

Table 1: Characteristics of grids used for the Gaussian pulse case.

Fig. 2 shows the error in L_2 norm with respect to the analytical solution at final time; the square root of the number of vertices is taken as a measure for the element size. It can be seen that the scheme converges correctly and the theoretical order of accuracy $p + 1$ featured by DGM is reached as long as the number of elements is sufficiently high. Fig. 3 shows the computation time required by the simulations, which vary linearly with the number of elements. By comparing both graphs, one can notice that for a given accuracy, using high order with a coarse grid is less CPU-intensive than using low order on a fine grid, i.e. high order is more efficient, as shown in Ref. [11]. For instance, the computation on grid 2 with $p = 6$ requires about 4.4 times less CPU time than the computation on grid 4 with $p = 3$, while achieving a comparable accuracy. The gain could even be substantially higher if a larger time step was used on coarser grids.

3.2 Acoustic Scattering by a Cylinder

To assess the impact of wall boundary treatments, the problem Nr. 2, Category 1 of the Second CAA Workshop on Benchmark Problems [23] is studied. It consists in the scattering of a Gaussian pressure pulse by a cylinder. An analytical solution is available for this case.

The computational domain sketched in Fig. 4 is a disc with a non-dimensional diameter of 20, containing a cylinder of diameter 1 centered at the origin. The initial conditions are:

$$p|_{t=0} = \rho|_{t=0} = e^{-(\ln 2) \frac{(x-4)^2+y^2}{0.2^2}}$$

$$u_1|_{t=0} = u_2|_{t=0} = 0$$

Mean flow velocity is set to zero and simulations are run until a non-dimensional time of $t = 10$. For each computation, the time step is set to the highest value not affecting the stability.

The influence of geometry discretization and wall boundary treatment is investigated; grid characteristics are summarized in Table 2 and computational parameters can be found in Table 3. To assess the effect of these parameters on the quality of the solution, pressure is monitored at point $(0, 5)$ and compared with the

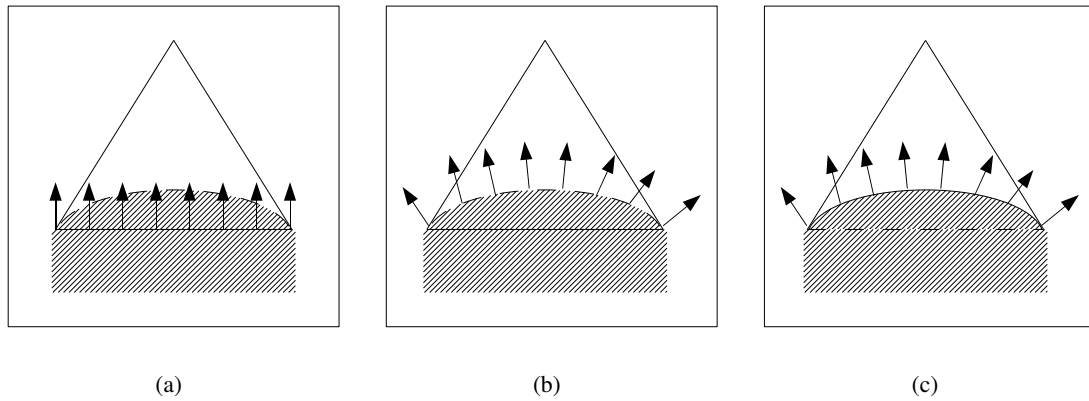


Figure 1: Illustration of the linear boundary treatment (a), the mixed boundary treatment (b) and the quadratic boundary treatment (c). The arrows represent the normals \mathbf{n} used for prescribing the zero-normal-velocity condition, solid lines are the element boundaries on which the flux is integrated.

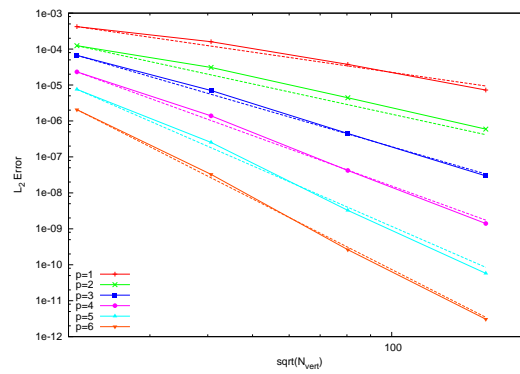


Figure 2: L_2 error at $t = 20$ over the computational domain for the Gaussian pulse problem, in function of the square root of the number of vertices N_{vert} . Solid lines are numerical results for values of p from 1 to 6, dashed lines represent the slopes for the corresponding theoretical order of accuracy $p + 1$.

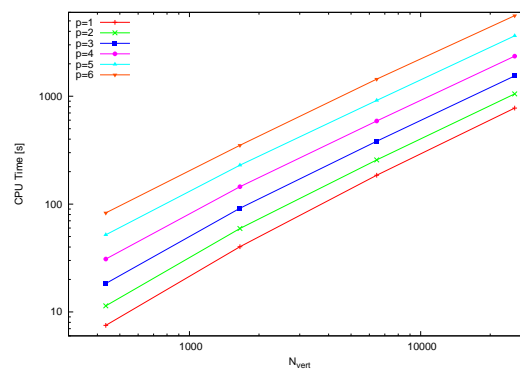


Figure 3: CPU time required by the computations for the Gaussian pulse problem, in function of the number of vertices N_{vert} , for values of p from 1 to 6.

| Grid Name | C4 | C8 | C12 | C16 |
|--------------------------|------|------|------|------|
| Vertices on the Cylinder | 4 | 8 | 12 | 16 |
| Vertices | 1077 | 1084 | 1279 | 1494 |
| Elements | 2154 | 2168 | 2558 | 2988 |

Table 2: Characteristics of grids used for the acoustic scattering case.

| Test Case Name | Grid Name | p | Bnd. Treatment |
|----------------|-----------|-----|----------------|
| C4P2L | C4 | 2 | Linear |
| C4P2Q | C4 | 2 | Quadratic |
| C4P4L | C4 | 4 | Linear |
| C4P4Q | C4 | 4 | Quadratic |
| C4P6L | C4 | 6 | Linear |
| C4P6M | C4 | 6 | Mixed |
| C4P6Q | C4 | 6 | Quadratic |
| C8P6L | C8 | 6 | Linear |
| C8P6M | C8 | 6 | Mixed |
| C8P6Q | C8 | 6 | Quadratic |
| C12P6L | C12 | 6 | Linear |
| C16P2L | C16 | 2 | Linear |
| C16P4L | C16 | 4 | Linear |
| C16P6L | C16 | 6 | Linear |

Table 3: Computation parameters used for the acoustic scattering problem.

analytical solution. The reference solution features a first maximum at about $t = 6.3$, corresponding to the direct field, and a second maximum at $t = 8.2$, corresponding to the scattered field.

Fig. 5 shows the results of computations with varying values of p and linear boundary treatment on grids C4 and C16. On grid C16, the results converge towards the reference solution with p-refinement for both direct and scattered fields. On grid C4, increasing p allows to correctly resolve the direct pulse, but does not eliminate the large error in phase and amplitude for the scattered field. At high order, the accuracy is thus limited by the rough modelling of the cylinder.

Fig. 6 shows the improvement of the solution for the scattered field with grid refinement at $p = 6$. For $7.7 < t < 8.7$, one can observe a phase lag between the numerical results and the reference solution, which is reduced on finer grids. It can be explained by the distance ΔL between the linear geometry representation and the exact geometry, as sketched in Fig. 7; this difference in travel distance for acoustic waves becomes obviously smaller when refining the grid.

Fig. 8 indicates how the error is affected by the "mixed" wall treatment on grids C4 and C8. This treatment does not reduce the phase error for $7.7 < t < 8.7$ compared to the linear treatment, because it does not correct the poor geometry description. However, for $t > 8.7$, the error on grid C8 seems to be dominated by scatter directivity, which is improved by the quadratic treatment of normals.

Fig. 9 puts in evidence the great improvement brought by the use of curved boundary treatment on the coarse grid C4: as the cylinder geometry is represented exactly by the quadratic boundary, the phase error is suppressed. This is the reason why the solution for case C4P6Q is even more accurate than results obtained on refined grids with other boundary treatments, as shown in Table 4.

However, it should be mentioned that the use of curved high-order elements, can affect the stability of the scheme. Indeed, the stability limit depends on the element size and p through the condition on the CFL number. The maximum time step required to run a stable computation can thus be lower with the quadratic boundary treatment than with the linear and mixed treatments. Nevertheless, Table 5 shows that this limitation is significant only for elements with very high curvature and at high order, like in the case C4P6Q.

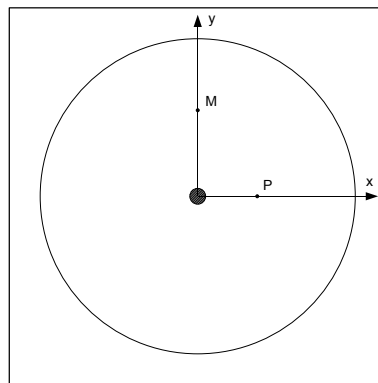


Figure 4: Computational domain for the acoustic scattering problem. P (4,0) is the center of the pulse at initial time, M (0,5) is the point where the pressure is monitored.

4 Conclusion

In this work, DGM is applied to the 2D LEE on unstructured triangular meshes in order to simulate aeroacoustic propagation. The quadrature-free form of DGM is used to achieve a low computational cost. The

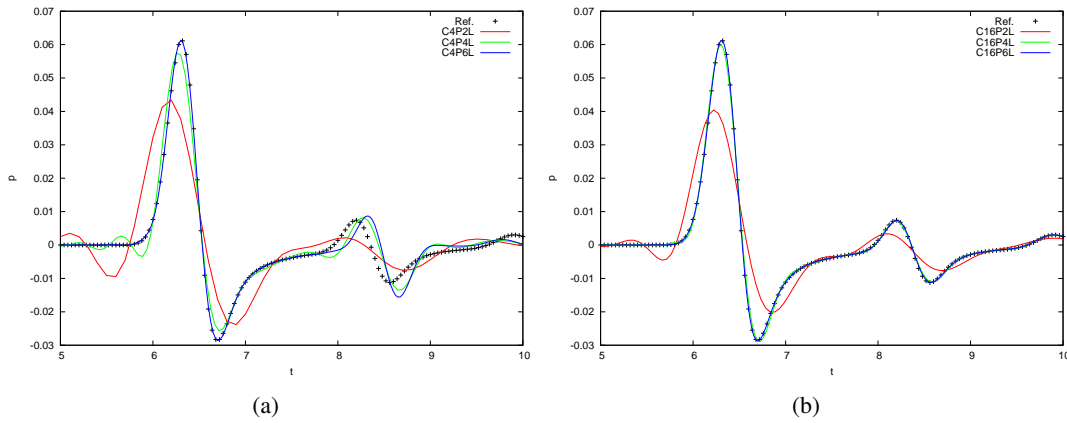


Figure 5: Pressure at point (0,5) with linear boundary treatment on grids C4 (a) and C16 (b) for the acoustic scattering problem: comparison between $p = 2$, $p = 4$ and $p = 6$.

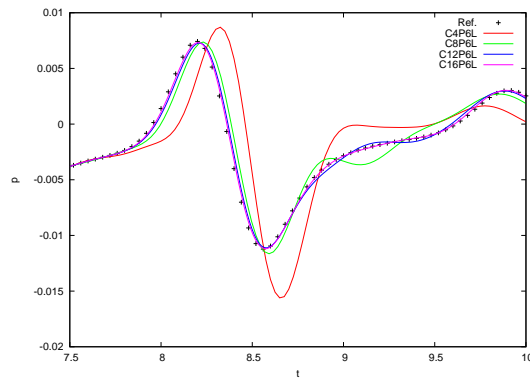


Figure 6: Pressure at point (0,5) with $p = 6$ and linear boundary treatment for all grids used in the acoustic scattering problem.

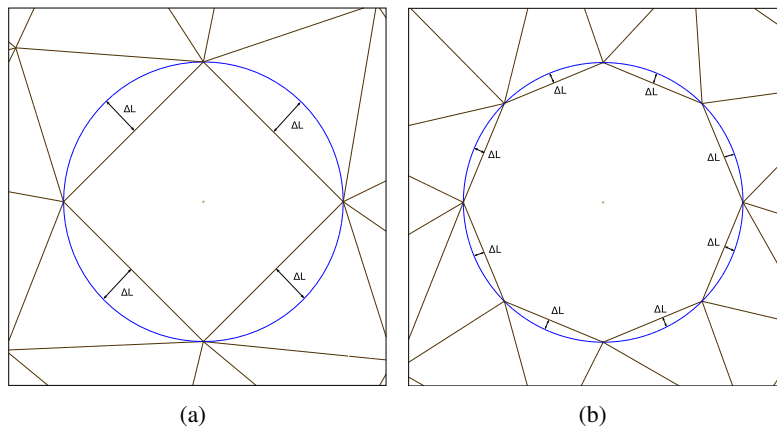


Figure 7: Details of grids C4 (a) and C8 (b) close to the cylinder for the acoustic scattering problem. ΔL represents the distance between the straight boundary edges and the exact geometry.

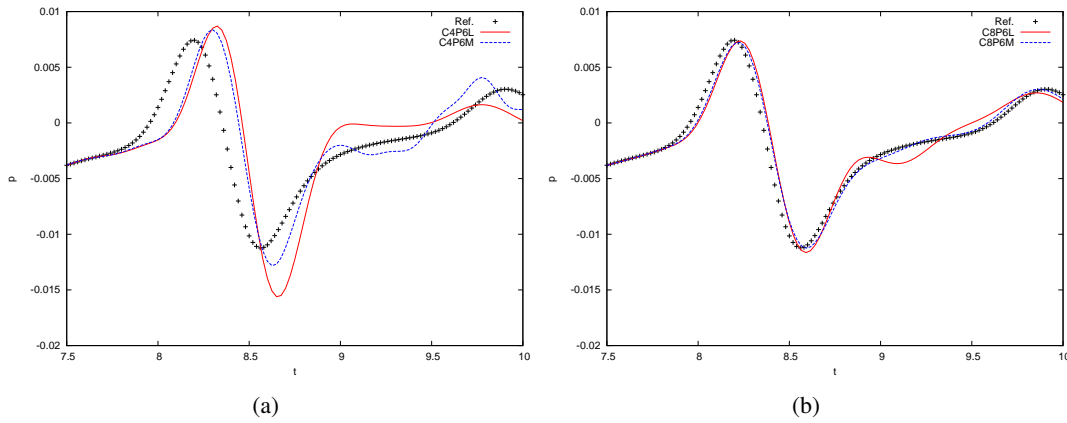


Figure 8: Pressure at point (0,5) with $p = 6$ on grids C4 (a) and C8 (b) for the acoustic scattering problem: comparison between the linear boundary treatment and the mixed boundary treatment.

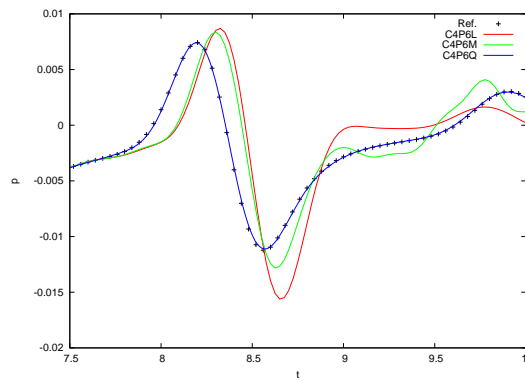


Figure 9: Pressure at point (0,5) with $p = 6$ and different boundary treatments on grid C4 for the acoustic scattering problem.

| Case Name | C4P6L | C4P6M | C4P6Q | C8P6L | C8P6M | C12P6L | C16P6L |
|-----------|----------------------|----------------------|--|----------------------|----------------------|----------------------|----------------------|
| Error | $2.83 \cdot 10^{-5}$ | $1.65 \cdot 10^{-5}$ | $2.23 \cdot 10^{-8}$ | $2.51 \cdot 10^{-6}$ | $1.38 \cdot 10^{-6}$ | $4.50 \cdot 10^{-7}$ | $1.31 \cdot 10^{-7}$ |

Table 4: L_2 error in pressure at point (0,5) over the time interval $[7.5, 10]$ for some cases with $p = 6$ of the acoustic scattering problem.

| Grid and Order | Time Step (Linear Wall Treatment) | Time Step (Quadratic Wall Treatment) |
|------------------|-----------------------------------|--------------------------------------|
| Grid C4, $p = 2$ | 0.10 | 0.088 |
| Grid C4, $p = 4$ | 0.046 | 0.028 |
| Grid C4, $p = 6$ | 0.025 | 0.013 |
| Grid C8, $p = 6$ | 0.024 | 0.024 |

Table 5: Comparison of maximum time steps with linear and quadratic boundary treatments for the acoustic scattering problem.

accuracy of the method can be efficiently controlled by freely specifying the order of the underlying polynomial basis, without affecting the compactness of the scheme.

The application to the propagation of a Gaussian pressure pulse in a quiescent medium allows to verify that the implementation reaches the theoretical order of accuracy of DGM and shows that the method is computationally more efficient at high order. However, the simulation of acoustic scattering by a cylinder demonstrates that accuracy at high order can be limited by the linear treatment of curved geometries.

The "mixed" treatment consisting in prescribing wall boundary conditions with normals to the quadratic geometry, while integrating over elements with straight edges, results in an improvement, but does not reduce the local phase error. This error is eliminated by the full quadratic treatment which involves curved elements. The latter requires more memory storage because it is incompatible with the quadrature-free technique, but the total overhead is not prohibitive, as such elements only have to be used in the vicinity of curved wall boundaries.

Highly curved elements used near convex geometries are smaller than elements with straight edges, which leads to reduced time steps, because of stability conditions on explicit time integration schemes. However, if high accuracy is needed, the full quadratic treatment is necessary to take advantage of the arbitrary order featured by DGM, without the burden of re-meshing.

The 2D cylinder considered in the present work can be represented exactly by a quadratic curve for which an analytical expression is available. However, this may not be the case for more realistic applications, where the geometry is usually modeled by CAD systems or built from basic geometrical entities available in the meshing software. If the mesher is not able to output high-order geometry information, dedicated methods are then needed to accurately reconstruct curved boundaries from mesh points. The implementation of such algorithms into the solver is not straightforward, particularly in 3D, and could be the subject of future work.

Acknowledgments

Thomas Toulorge acknowledges the financial support of the European Commission through the Marie-Curie Research and Training network "AETHER", Contract Nr. MRTN-CT-2006-035713.

References

- [1] T. Colonius, S.K. Lele, *Computational aeroacoustics: progress on nonlinear problems of sound generation*, Progress in Aerospace Sciences, Vol. 40, pp. 345–416, 2004.
- [2] W. H. Reed, T. R. Hill, *Triangular mesh methods for the neutron transport equation*, Los Alamos Scientific Laboratory, Technical report LA-UR-73-479, 1973.
- [3] H. Atkins, C.-W. Shu, *Quadrature-Free Implementation of the Discontinuous Galerkin Method for Hyperbolic Equations*, AIAA Journal, Vol. 36, pp. 775-782, 1998.
- [4] F. Q. Hu, H. L. Atkins, *Two-dimensional Wave Analysis of the Discontinuous Galerkin Method with Non-Uniform Grids and Boundary Conditions*, 8th AIAA/CEAS Aeroacoustic Conference, Breckenridge, CO (2002), AIAA Paper Nr. 2002-2514.
- [5] F. Q. Hu, M. Y. Hussaini, P. Rasetarinera, *An Analysis of the Discontinuous Galerkin Method for Wave Propagation Problems*, Journal of Computational Physics, Vol. 151, pp 921-946, 1999.
- [6] R. Hagmeijer, C.P.A. Blom, H.W.M. Hoeijmakers, *Wave-Speed Analysis of Discontinuous Galerkin Finite Element Method for Aeroacoustics*, ECCOMAS Computational Fluid Dynamics Conference 2001, Swansea, Wales, U.K., 4-7 September 2001.

- [7] M. Ainsworth, P. Monk, W. Muniz, *Dispersive and Dissipative Properties of Discontinuous Galerkin Finite Element Methods for the Second-Order Wave Equation*, Journal of Scientific Computing, Vol. 27, pp. 5-40, 2006.
- [8] N. Chevaugeon, J.-F. Remacle, X. Gallez, P. Ploumhans, S. Caro, *Efficient Discontinuous Galerkin Methods for solving acoustic problems*, 11th AIAA/CEAS Aeroacoustics Conference, Monterey (2005), AIAA paper 2005-2823, 2005.
- [9] N. Chevaugeon, K. Hillewaert, X. Gallez, P. Ploumhans, J.-F. Remacle, *Optimal numerical parameterization of discontinuous Galerkin method applied to wave propagation problems*, Journal of Computational Physics, Vol. 223, pp. 188-207, 2007.
- [10] Y. Reymen, M. Baelmans, W. Desmet, *Study of convergence and efficiency of a nodal Quadrature-Free Discontinuous Galerkin Method on meshes of tetrahedral and hexahedral elements*, International Conference On Spectral and High Order Methods, Beijing, China, 2007.
- [11] Y. Reymen, M. Baelmans, W. Desmet, *On the Performance of the Quadrature-Free Discontinuous Galerkin Method on Hexahedral and Tetrahedral Grids for Linearized Euler Equations*, 14th AIAA/CEAS Aeroacoustics Conference, Vancouver (2008), AIAA Paper Nr. 2008-3001, 2008.
- [12] J.S. Hesthaven, T. Warburton, *Nodal High-Order Methods on Unstructured Grids*, Journal of Computational Physics, Vol. 181, pp. 186-221, 2002.
- [13] C.P.A. Blom, *Discontinuous Galerkin method on tetrahedral elements for aeroacoustics*, PhD thesis, University of Twente, Enschede, 2003.
- [14] P.P. Rao, *High Order Unstructured Grid Methods for Computational Aeroacoustics*, PhD thesis, Pennsylvania State University, 2004.
- [15] M. Dumbser, C.-D. Munz, *ADER discontinuous Galerkin schemes for aeroacoustics*, C. R. Mecanique 333, pp. 683-687, 2005.
- [16] F. Bassi, S. Rebay, *High-order accurate discontinuous finite element solution of the 2D Euler equations*, Journal of Computational Physics 138, pp. 251-285, 1997.
- [17] L. Krivodonova and M. Berger, *High-order Accurate Implementation of Solid Wall Boundary Conditions in Curved Geometries*, Journal of Computational Physics, Vol. 211, pp. 492-512, 2006.
- [18] H.L. Atkins, *Continued development of the discontinuous Galerkin method for computational aeroacoustic applications*, AIAA paper. 97-1581, 1997.
- [19] Y. Reymen, M. Baelmans, W. Desmet, *A 3D Discontinuous Galerkin Method for Aeroacoustic Propagation*, 12th International Congress on Sound and Vibration, Lisbon, 2005.
- [20] J. S. Hesthaven, *From Electrostatics to Almost Optimal Nodal Sets for Polynomial Interpolation in a Simplex*, SIAM Journal on Numerical Analysis, Vol. 35, pp. 655-676, 1998.
- [21] M.H. Carpenter, C.A. Kennedy, *A fourth-order 2N-storage Runge-Kutta scheme*, NASA TM 109112, 1994.
- [22] C.K.W. Tam, J.C. Webb, *Dispersion relation preserving finite difference schemes for computational acoustics*, Journal of Computational Physics, Vol. 107, pp. 262-281, 1993.
- [23] C.K.W. Tam, J.C. Hardin (Eds.), *Second Computational Aeroacoustics Workshop on Benchmark Problems*, NASA Conference Paper Nr. 3352, 1997.